SOFT ROBOTICS
Volume 00, Number 00, 2020

DOI: 10.1089/soro.2019.0055

SoRo
Soft Robotics

Tapered Polymer Whiskers to Enable Three-Dimensional Tactile Feature Extraction

David W. Collinson,[1,*] Hannah M. Emnett,[1] Jinqiang Ning,[1,†] Mitra J.Z. Hartmann,[1,2] and Lynda Catherine Brinson[3]

Abstract

Many mammals use their vibrissae (whiskers) to tactually explore their surrounding environment. Vibrissae are thin tapered structures that transmit mechanical signals to a wealth of mechanical receptors (sensors) located in a follicle at each vibrissal base. A recent study has shown that—provided that the whisker is tapered—three mechanical signals at the base are sufficient to determine the three-dimensional location at which a whisker made contact with an object. However, creating biomimetic tapered whiskers has proved challenging from both materials and manufacturing standpoints. This study develops and characterizes an artificial whisker for use as part of a sensory input device that is a biomimic of the biological rat whisker neurosensory system. A novel manufacturing process termed surface conforming fiber drawing (SCFD) is developed to produce artificial whiskers that meet the requirements to be a successful mechanical and geometric mimic of the biological rat vibrissae. Testing the sensory capabilities of the artificial whisker shows improved performance over previous nontapered filaments. SCFD-manufactured tapered whiskers demonstrate the ability to predict contact point locations with a median distance error of 0.47 cm.

Keywords: whisker, vibrissa, active sensing, tapered filament, biomimetic, drawing

Introduction

VIBRISSAE, ALSO CALLED WHISKERS, are long tapered hairs that serve as important sensors for many mammals. In particular, many species of rodents use their vibrissae for active tactile sensing to locate and explore objects in their surroundings.[1–9] A whisker has no sensors along its length. Instead, all sensors (receptors) are located in a densely innervated follicle at the whisker base. Deformations of the whisker are mechanically transmitted to these receptors, which in turn transduce the mechanical signals to electrical signals for subsequent neural processing. To withstand repeated large deformations, vibrissae are tough, stiff, and elastic.

In the field of robotics, artificial whiskers have been used to determine three-dimensional (3D) contact point locations and to extract two-dimensional (2D) and 3D object contours.[10–15] Robotic systems incorporating whiskers could be used to help explore remote and/or spatially constrained locations, to enable sensing on biomedical devices (e.g., catheters), to help stabilize drones,[16] and to complement optical (camera or light detection and ranging [LIDAR]) systems when illumination is challenging or undesirable (e.g., in fog or glare, or in stealth applications).[17]

The mechanical response of an artificial whisker on a robotic system will depend on both its geometry and its material properties. Given that biological vibrissae have geometric and material properties well suited for tactile sensing, it seems reasonable to develop artificial whiskers based on mimicking (perhaps at scale) the geometric and mechanical properties of their biological counterparts.

However, several factors make this type of biomimetic approach particularly challenging. Multiple studies have indicated that taper is a particularly important feature for whisker-based sensing.[12,18,19] The taper requirement eliminates conventional drawing or extrusion procedures, which

[1]Department of Mechanical Engineering, Northwestern University, Evanston, Illinois, USA.
[2]Department of Biomedical Engineering, Northwestern University, Evanston, Illinois, USA.
[3]Department of Mechanical Engineering and Materials Science, Duke University, Durham, North Carolina, USA.
*Current affiliation: Department of Mechanical Engineering and Materials Science, Duke University, Durham, North Carolina, USA.
†Current affiliation: George W. Woodruff School of Mechanical Engineering, Georgia Institute of Technology, Atlanta, Georgia, USA.

typically produce continuous cylindrical filaments. In addition, the small diameter at the tip of a tapered whisker poses a challenge for standard casting and molding techniques. Materials that are stiff enough to resemble biological whisker material are typically too viscous (even when melted) to flow through mold geometries only tens of microns in diameter.

Previous studies have used several different materials and manufacturing techniques to produce artificial whiskers for sensing.[20–23] Although these previous solutions have produced functional devices, none to date has successfully recreated both the geometric and mechanical properties of a rat vibrissa.

There are limited examples of previous attempts to produce functional linearly tapered polymer structures in the scientific literature, highlighting the manufacturing challenges.[18,24,25] The tactile sensing system ''Cillia'' developed by Ou *et al.*[24] uses stereolithography (SLA) techniques to produce a bed of hairs built from 50 μm voxels. However, hairs produced by ''Cillia'' are a stacked series of voxels (thus a nonsmooth taper) that reflects the additive manufacturing process used. The process is also limited in the length of hairs it can produce and only photocurable materials can be used. In addition to ''Cillia'' there are also commercial examples of tapered filaments in applied systems.

Several patents detail the production of artificial tapered hairs from polyamide for use in paintbrushes.[25,26] However, the manufacturing technique outlined in this patent is limited in material choice and achievable aspect ratios. Another technique used solvent to remove material from a filament while it was drawn out of a bath.[27] Again, material choice is limited, and the chemical treatment process may affect the integrity of the filament and its properties.

Multiple previous studies have produced whiskers that are incorporated into a robot and have been successfully used as sensory whisking devices. However, in the case of Fox *et al.*[21] and Pearson *et al.*,[22] the use of fiberglass composites leads to whiskers that are far stiffer ($\approx$15 GPa) compared with the biological vibrissae and requires molding steps, which limits the taper and minimum tip diameter achievable. Alternatively, the use of SLA by Sullivan *et al.*[23] limits material choice to photocurable resins. Although the improved resolution of SLA and fused deposition modeling (FDM) allow for smaller tip diameters, the slow build time, digital profile, and low fracture toughness limit the whisker's application as a functional and durable sensor.[20,23] In addition, the size of the produced whisker is constrained by the build volume of the printer.

In this study, we present a novel manufacturing technique termed surface conforming fiber drawing (SCFD). When used with a polycarbonate (PC) that has been modified for FDM, SCFD can produce a scaled near-biomimetic model of a rodent vibrissa. We use SCFD to create 5$\times$ scale biomimics of rostral (short) and caudal (long) whiskers from a Long Evans rat, and demonstrate that these whiskers are durable and have material properties similar to those of biological vibrissae. Specifically, three-point bending analysis indicates that the SCFD drawing process causes the material modulus to increase along the whisker length in a way that mimics the increase in bending stiffness observed in the biological vibrissae. Finally, we show that SCFD-manufactured whiskers (with taper) can more accurately determine 3D contact point locations than artificial whiskers of the same material without taper. Future study will aim to further develop the manufacturing procedure to allow for more accurate control and prediction of artificial whisker properties.

Materials and Methods

Specification of desired artificial whisker properties

The mechanical response of a whisker to a deflection depends on both its material properties and its geometry. Typical dimensions and elastic material properties of a biological vibrissa are given in Figure 1a. A rat vibrissa typically has an arclength (S) between 10 and 50 mm and a base diameter (D_{base}) between 60 and 200 μm. The diameter tapers approximately linearly to a tip diameter (D_{tip}) of 5 μm or less. Figure 1A also illustrates the three main material regions of the whisker. The bulk of the whisker is the cortex.[28–30] A protective outer layer called the cuticle surrounds the cortex.[31] The medulla is a highly porous core[31,32] that follows strict geometric rules relative to the geometry of the entire whisker. Specifically, for rat vibrissa, the medulla arclength (S_{med}) and base diameter (D_{med}) are given by $S_{med} = 0.95S - 7.3$ mm and $D_{med} = 0.44D_{base} - 0.019$.[27]

Previous simulation study has shown that whisker taper is critical to ensuring that the 3D contact point can be determined accurately based on three signals at the whisker base.[12] The biological whisker taper is quantified by the metric radius slope,[32] $Slope_R$, defined as

$$Slope_R = \frac{R_{base} - R_{tip}}{S} \tag{1}$$

where R_{base} is the base radius, R_{tip} is the tip radius, and S is the whisker arclength.

Biological whiskers typically have a $Slope_R$ between 0.001 and 0.003,[32] and a successful manufacturing procedure will produce artificial whiskers with a $Slope_R$ within this range. The targeted dimensions of the artificial whisker in Figure 1b are determined by scaling the biological vibrissa dimensions by a factor of 5, chosen so that the whiskers can be easily incorporated into macroscale robotic follicles. Microscale robotic devices were not considered.

The specifications are such that the dynamic behavior of the biological whisker will be successfully replicated in the artificial whiskers. The interwoven requirements involved with manufacturing these whiskers are presented in Figure 1c. The success of a chosen solution depends on striking a balance between the desired material properties, the manufacturing process, and the performance of the produced whisker. The specifications of the engineered rat whisker include geometric constraints as well as careful selection of the material properties to obtain the desired static and dynamic response. Each of these is mentioned in turn as follows.

An elastic response without permanent deformation to a static load is essential to allow the manufactured whisker to function as part of a robotic device, sustain deflections, and operate in a variety of environmental conditions. To mimic a biological rat whisker the artificial whisker should be able to sustain at least a 50° deflection elastically[19,33] (fully reversible deformation) and undergo repeated deflections in all orientations without significant fatigue or creep. The Young's modulus of biological vibrissae has been previously measured

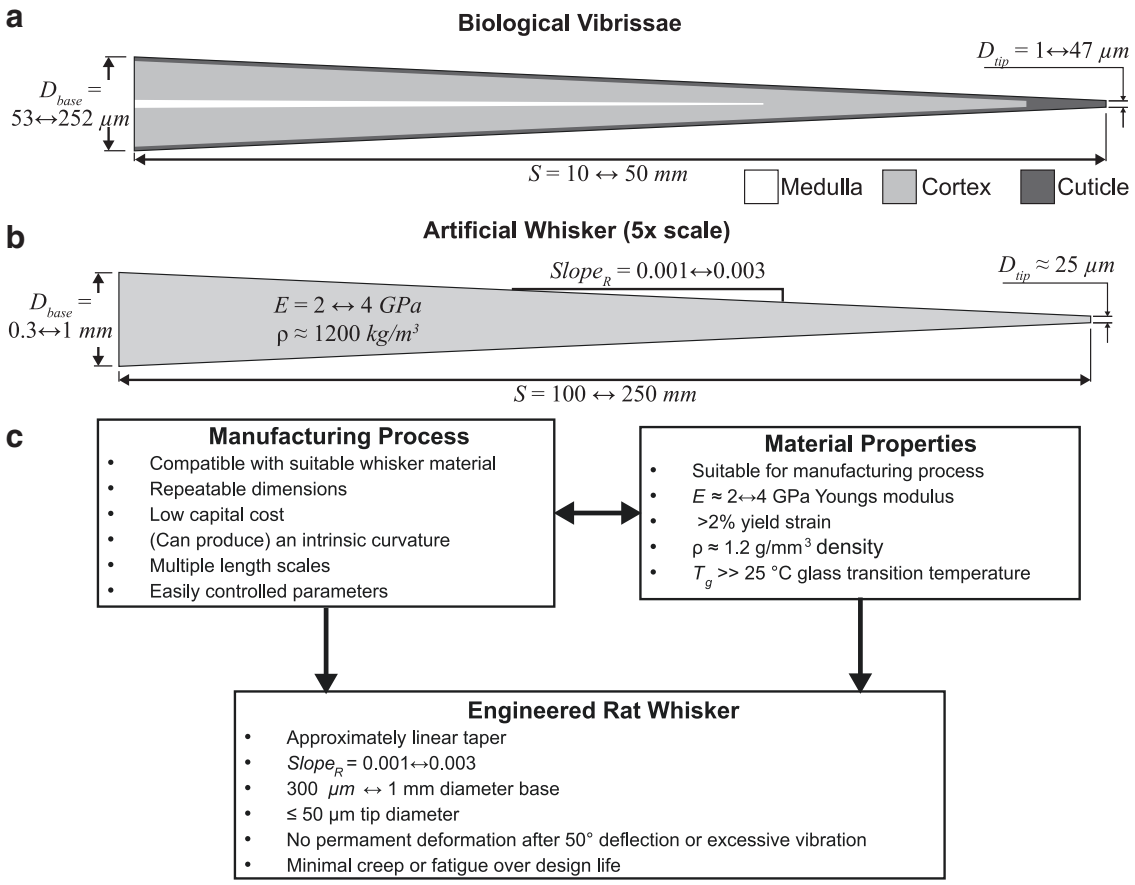

FIG. 1. Geometric, static, and dynamic specifications for the engineered rat whisker. **(a)** A schematic illustrates typical ranges for the dimensions of a rat whisker. **(b)** Schematic of required geometric and material properties for artificial whisker 5×larger than caudal and rostral vibrissae. **(c)** Engineering design problem with the competing design requirements detailed. D_{base}, base diameter; D_{tip}, tip diameter; S, arclength.

to be from 2.9 to 5.0 GPa, with an increase in the measured modulus near the whisker tip.[34–36] The modulus of the artificial whisker will need to be on a similar order of magnitude. An important factor of static performance will also be how the whisker is mounted to the electronic sensory system and successful transmission of mechanical deformation along its length to the sensors located at its base. Further consideration of these aspects to a whisker sensory device can be found in the study by Emnett *et al.*[11]

Finally, the dynamic properties of the whisker will control how the whisker behaves during and after a deflection. An artificial whisker must have a short relaxation time so that the whisker can quickly return from a deflection. However, if the whisker does not have sufficient intrinsic damping, then excessive vibration could occur after a deflection, introducing noise into a transmitted force signal. These constraints mean choosing a polymer with a glass transition temperature (T_g) much greater than room temperature to allow the polymer to operate in the glassy regime while minimizing vibration at room temperature.

Keratin, the primary component of biological vibrissae, has a loss tangent at room temperature[37] that ranged between tan $\delta = 0.02$–0.03, which should be a suitable target value. Using a material with a T_g much greater than room temperature is also beneficial for ensuring that the dynamic response is consistent across a range of operating temperatures and timescales.

Material selection

We considered a range of thermoplastic and thermoset polymers (Table 1), including both conventional engineering polymers, as well as filaments commercially developed for FDM.[38,39] This initial range of choices was determined by comparing each material's properties, as provided by the manufacturer, to the desired material properties (Fig. 1).

The advantage of using commercial polymers developed for FDM is that they include plasticizers to improve their ability to flow when melt compared with traditional engineering polymers.[40,41] At the same time, the number of FDM-compatible filaments with mechanical properties appropriate for biomimetic whiskers is fairly limited, because the plasticizers that permit 3D printing also often reduce the modulus of the material. In addition, if the plasticizers are immiscible with the polymer, then multiphase materials can result, complicating the processing–structure–property relationship.[42]

We selected four materials from Table 1 for further testing, each of which met the design criteria in Figure 1. From material property data sheets provided by the manufacturers, we identified PC, polysulfone, Polymaker® PC-Max™, and Stratasys® ABSplus-P430 (ABS) as the materials that best met design requirement and were most likely to be easily processed into tapered whiskers able to

Table 1. Review of Commonly Available Thermoplastics

Conventional engineering polymers				
Material	*Elongation at break/ yield strain (%)*	*Elastic modulus (GPa)*	*Glass transition temperature, T_g (°C)*	*Density (g/cc)*
Polysulfone[c]	50–100/—	2.48	185–266	1.24
Polyphenylsulfone[d]	60–120/7.2	2.34	220	1.29
ABS/PC alloy[e]	>10/—	2.76	125	0.90–1.40
Extruded PC[f]	>50/6	2.40	145	1.19
PEEK[g]	68/—	3.19	142	1.27
Epoxy resin[h]	1–2/—	3–5	—	1.2–1.3
PEI[i]	60/7.0	3.0	219	1.30
Desired	>3	2–4	>>25	0.8–1.6

Materials developed for FDM					
Material	*Elongation at break/ yield strain (%)*	*Elastic modulus (GPa)*	*T_g (°C)*	*Density (g/cc)*	*Printing temp (°C)*
Polymaker PC-Max[j]	12.2/—	2.05	113	1.18–1.20	250–270
Polymaker PC-plus[k]	3.2/—	2.31	113	1.19–1.20	250–270
Stratasys ASA[l]	9/2	1.95	108	1.05	—
Stratasys ABSplus-P430[m]	6/2	2.20	108	1.04	—
Desired	>>3/>3	2–4	>>25	0.8–1.6	<260

Manufacturer-listed properties of conventional engineering polymers and filaments developed for FDM.[a,b]
Manufacturer-listed properties of conventional engineering polymers and filaments developed for FDM.[a,b]
[a]Polymers chosen for assessment are in ***bold italic.***
[b]Values that are missing from the datasheet for each thermoplastic are indicated with a dash (—).
[c]Solvay, Ltd. Udel P-3500 Technical Data Sheet, 2013. Available from www.catalog.ides.com (accessed April 2019).
[d]Solvay, Ltd. Radel R-5600 Technical Data Sheet, 2014. Available from www.catalog.ides.com (accessed April 2019).
[e]RTP, Ltd. Polycarbonate-ABS Alloy (2500 A), 2006. Available from web.rtpcompany.com (accessed April 2019).
[f]Covestro, Ltd. Makrolon 2205 Technical Data Sheet, 2018. Available from www.plastics.covestro.com (accessed April 2019).
[g]Fried JR. Poly(ether ether ketone). In: Mark JE. (Ed). Polymer Data Handbook, 1st ed. Oxford University Press, 1999.
[h]Shelley MY. Epoxy resins. In: Mark JE. (Ed). Polymer Data Handbook, 1st ed. Oxford University Press, 1999.
[i]Tan L-S. Poly(ether imide). In: Mark JE. (Ed). Polymer Data Handbook, 1st ed. Oxford University Press, 1999.
[j]Polymaker, Ltd. PC-Max Technical Datasheet, 2018. Available from www.polymaker.com (accessed April 2019).
[k]Polymaker, Ltd. PC-Plus Technical Datasheet, 2018. Available from www.polymaker.com (accessed April 2019)
[l]Stratasys, Ltd. ASA Technical Datasheet, 2018. Available from www.stratasys.com (accessed April 2019)
[m]Stratasys, Ltd. ABSplus-P430 Technical Datasheet, 2017. Available from www.stratasys.com (accessed April 2019).
FDM, fused deposition modeling.

withstand large repeated elastic deformations. These materials are in ***bold italic*** in Table 1.

Baseline dynamic mechanical analysis sample creation

To form samples from the four stock materials for baseline mechanical testing, ~5 g of each material was heated at least 30°C past its glass transition temperature (T_g) and hot pressed for 30 min to form a thick film. The films were then annealed at 20°C above the T_g for each material and then trimmed to a size suitable for dynamic mechanical analysis (DMA) testing. The trimmed samples were then reannealed for another 24 h before testing. The properties of these simple films were then used as a baseline for understanding the properties of the drawn whiskers. The manufacturing method for the whiskers is described in detail in Results section.

For tensile viscoelastic measurements of possible materials, the sample films produced from the stock materials were strained to 0.1% strain at a frequency of 1 Hz while the temperature was ramped from room temperature to 140°C. Tensile quasistatic tests were conducted by straining the sample at a constant strain rate of 0.01 s^{-1} until the sample failed.

To test the mechanical properties of the manufactured whiskers, samples 30 mm in length were cut and mounted in a DMA (TA Instruments, New Castle). To obtain samples from manufactured whiskers for three-point bending analysis, the intended load points were marked at 50, 100, and 150 mm from the whisker base. Samples were then taken by cutting the whisker ~7.5 mm either side of the marked point to create a 15 mm long sample. Viscoelastic three-point bending tests were conducted by setting whisker samples in a three-point bending mount with a 10 mm span and subjecting them to a strain sweep from 0.001% to 1% strain. The bending modulus measured at 1% strain was used in subsequent analysis.

Geometric characterization

To obtain continuous profiles of the whisker geometry, whiskers were mounted on a black background next to a ruler for scale and then scanned at high resolution to digitize the whisker profile. A MATLAB® script was then

generated to discretize and measure the whisker diameter along the entire length of the whisker.

Atomic force microscopy

Because plasticizers could potentially form an immiscible polymer phase in the chosen materials, we performed atomic force microscopy (AFM) measurements of several artificial whisker cross sections. These measurements allowed us to determine whether there were any nanoscale variations in mechanical properties, and to investigate the impact of the manufacturing method on the existing microstructure. To prepare artificial whiskers for AFM, their length, and base and tip diameter were measured, and they were then cut into segments 60 mm long and mounted in epoxy (EpoxiCure® 2; Buehler, USA). The embedded whiskers were then allowed to cure overnight to produce an epoxy cylinder with an embedded whisker.

To expose a whisker cross section, the epoxy cylinder was freeze-fractured to create whisker segments $\sim$5–10 mm long, each from a different location along the length of the original whisker. The segments were then mounted in a vice, and a razor blade was used to carve away the epoxy around the exposed whisker cross section and create a $\sim 1\,mm^2$ area for facing off by an ultramicrotome. The exposed whisker cross section was faced off with a Leica SPF UC7 ultramicrotome at room temperature to create a surface with a roughness (R_a) between 30 and 40 nm.

A Bruker Icon® AFM was used to conduct PeakForce® quantitative nanomechanical mapping on the exposed cross sections. A TESPA-VW (Bruker, USA) cantilever with a nominal stiffness of 40 N/m was used. Before scans were taken, the deflection sensitivity, spring constant, and tip radius were all calibrated. Image quality degraded significantly after two to three scans were taken, and we speculate that this degradation was due to contamination of the AFM tip from the plasticizer. The AFM cantilever was replaced once image quality degraded.

Evaluation of whisker sensor quality

We compared the sensing capabilities of a tapered SCFD-fabricated whisker made of PC-Max with those of a cylindrical whisker constructed of the same material. Specially, we compared the degree to which the mechanical signals at the base of the tapered and cylindrical whiskers could be used to estimate the location of a 3D contact point to which the whisker had been deflected.

Following the approach of a previous study[11] we constructed a Maltese-cross-based artificial follicle that used strain gages to measure the magnitude and direction of deflections at the whisker base. Each arm of the cross corresponded to a half-Wheatstone bridge, so that four time-varying voltages described the whisker's bending. Each voltage was amplified with a gain of 1000 and filtered at 1.5 kHz before being digitally acquired with a 16-bit delta-sigma analog-to-digital converter with a modulator frequency of 3.4 MHz and an output data rate of 500 Hz. A PIC32 microcontroller acquired the data from the converter and then forwarded the data to MATLAB over USB.

We used a custom-built setup to deflect the whisker to specific locations in 3D space as shown in the schematics of Figure 2a–d. The experimental data set consisted of 192 unique whisker deflections to specific 3D contact points, designated in spherical coordinates as (r_{cp}, θ_{cp}, Φ_{cp}), where the subscript ''cp'' denotes ''contact point.'' These coordinates are illustrated in Figure 2b and 2d. The radial distance, r_{cp}, is the straight-line distance from the whisker base to the contact point. The angular deflection in the azimuthal (x–y) plane is denoted by θ_{cp} and the angular deflection in the elevation (x–z) plane is denoted by Φ_{cp}. This coordinate system differs from a standard spherical coordinate system only in that Φ_{cp} is measured from the x–y plane, not the z-axis. The whisker was tested at values of r_{cp} between 70 and 120 mm along the whisker length, and between ±20° in azimuth and elevation.

The identical artificial follicle was used to acquire data for both the cylindrical and tapered whisker. The follicle was

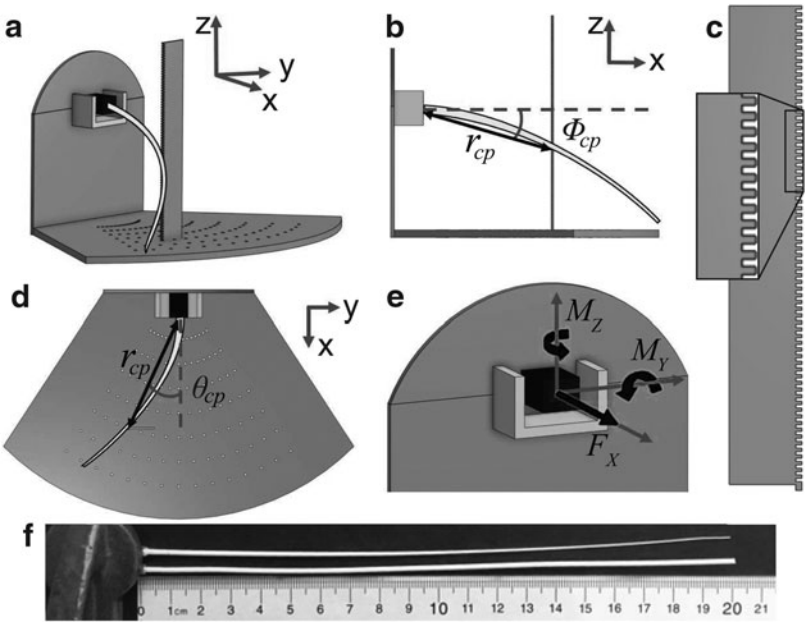

FIG. 2. Experimental setup. **(a)** A 3D schematic of the experimental setup illustrates deflection of a tapered whisker. **(b)** Side view schematic of experimental setup illustrates the variables r_{cp} and Φ_{cp}. **(c)** An expanded view (not to scale) of the apparatus used to hold the whisker at a fixed elevation with the *inset* showing the tooth structure. The whisker was held fixed within each of the toothed notches on the *right side*. **(d)** *Top view* schematic of the experimental setup illustrates the variables r_{cp} and θ_{cp}. **(e)** Illustration of the mechanical signals at the whisker base required for 3D contact point determination. **(f)** A photograph compares the tapered and cylindrical whiskers used in the experiments. Both whiskers were truncated to $\sim$197 mm in length. 3D, three-dimensional.

specifically designed to measure the bending moments, M_Y and M_Z, at the whisker base, as well as the axial force, F_X. The signal M_Y was computed as the difference in voltage between the strain gages on two opposite sides of the cross; the signal M_Z was computed as the voltage difference of the other strain gage pair. The axial force F_X was approximated as the sum of the absolute value of all of four voltages.[11] These mechanical signals (M_Y, M_Z, F_X) are illustrated in Figure 2e.

The signals M_Y and M_Z can be combined to form M_B, the magnitude of the bending moment, and M_D, the direction of the bending moment, according to Equations 2 and 3.

$$M_B = \sqrt{M_Y^2 + M_z^2} \tag{2}$$

$$M_D = \text{atan}\left(\frac{M_Z}{M_Y}\right) \tag{3}$$

This triplet of mechanical signals, (M_B, M_D, F_X), has been shown in simulation to exhibit a unique, one-to-one mapping to all possible locations of the 3D whisker-object contact point (r_{cp}, θ_{cp}, Φ_{cp}) for a whisker with or without intrinsic curvature, provided that the whisker has taper.[12]

We deflected the whisker to each of the 192 contact points and held it stationary for 200 ms while continuously recording from the artificial follicle. The four time-varying voltages from the sensor were centered, normalized between −1 and 1, and then averaged for the 200 ms hold duration so that exactly four (time-averaged) voltage values were associated with each 3D contact point. From these four voltages we computed M_B, M_D, and F_X, and then normalized each of those three signals between −1 and 1 for all trials. Thus, each of the 192 deflections was associated with a known 3D contact point (r_{cp}, θ_{cp}, Φ_{cp}) as well as experimentally measured, normalized values for the mechanical signals (M_B, M_D, F_X).

Two different PC-Max whiskers were tested, both shown in Figure 2f. The cylindrical whisker was stock filament, and the tapered whisker was manufactured using the SCFD process. The stock filament was provided in a spool that caused the filament to have curvature. Therefore, before testing, the stock filament was annealed in an oven under tension until it was straight.

Scaling for the two PC-Max whiskers was constrained by the diameter of the stock filament, fixed at 1.7 mm. As shown in Table 2, the cylindrical whisker had an approximately constant radius of 1.7 mm (plus or minus variation in diameter of the stock filament) and was truncated to the match the approximate length of the 5× whiskers used in the materials section of the study ($\sim$197 mm).

Because the SCFD manufacturing process is new and, therefore, not yet highly repeatable, we were not able to precisely select the tip diameter for the tapered whisker. Instead we ensured that (1) the length of the tapered whisker matched that of the cylindrical whisker, and (2) the taper of the whisker was within biological range. We made this second choice because a previous study has shown that taper has a particularly large influence on the whisker's sensing capabilities.[12,19,43] The SCFD-manufactured whisker had a base diameter of 1.67 mm, a length of 197 mm, and a tip diameter of 0.47 mm, yielding a radius slope (Eq. 1) of 0.0031.

The tapered whisker can be compared with a biological whisker as follows: an example whisker from the third column of the E row of the rat vibrissal array has a base diameter of 174 μm, a tip diameter of 9 μm, and an arclength of 25.6 mm, yielding a radius slope of 0.0032 (Ref.[29]). The artificial tapered whisker can thus be thought of as a E3 whisker, ''barbered'' (truncated) to about 74% of its length ($\sim$18.9 mm), and then scaled by a factor of $\sim$10.

In addition to performing hardware experiments, we also conducted simulations for each of the 192 whisker deflections. These simulations served two purposes: they generated ''ground truth'' mechanical signals for each deflection position and they verified that a tapered whisker with the chosen geometry could generate forces and moments that uniquely map to the 3D contact point. All simulations used previously published quasistatic whisker bending software.[44] The inputs to the simulation were the geometry of the specific whisker and Young's modulus, set to 3.0 GPa. The outputs of the simulations were the six mechanical signals at the whisker base, including M_Y, M_Z, and F_X. The output of the simulations was normalized in the same way as the experimental data.

Using random forest regression in Python, we created a mapping between the 3D contact point (r_{cp}, θ_{cp}, Φ_{cp}) and the mechanical signals (M_B, M_D, F_X) obtained from simulations. No experimental data were used to generate the mapping. We then tested the uniqueness of the mapping using signals obtained from the artificial follicle. Contact point locations with θ_{cp} or Φ_{cp} <5° were excluded during training to help account for the anticipated range of the sensor ''dead-band,'' in which we expected mechanical signals to be below the sensitivity threshold of the sensor, given the radial distances tested.

The algorithm was trained on 98% of the simulation data set and limited to a maximum depth of 30% of the input data set's length to create a ''lookup table.'' The mapping data set was generated 100 times and the data set with the highest correlation coefficient for the radial distance was used during testing. Mean square error was used to evaluate the quality of the mapping. We evaluated the predictive ability of the sensor using the full experimental data set.

Results

This study describes the development and characterization of a biomimetic whisker suitable for use as a sensory device. With the four candidate materials chosen and whisker

Table 2. Properties of Different PC-Max Whiskers Tested Using the Artificial Sensor

Profile	*Arclength,* S *(mm)*	*Base diameter,* D_{base} *(mm)*	*Tip diameter,* D_{tip} *(mm)*	*Bending modulus,* E_b *(GPa)*	*Manufacturing method*
Cylindrical	195	1.74	1.71	1.88	Stock
Tapered	195	1.67	0.47	2.47[a]	SCFD

[a]Bending modulus is measured by averaging the bending modulus along the whisker according to Material Selection section.
SCFD, surface conforming fiber drawing.

specifications established, multiple manufacturing processes are investigated, and a novel drawing process termed SCFD is developed. The SCFD process is described and the PC (Polymaker PC-Max) originally developed for FDM is found to be the material that produces an artificial whisker that satisfies the most design specifications out of the available options. Finally, we use SCFD to create $5\times$ scale artificial whiskers that mimic the caudal and rostral whiskers of the Long Evans rat, investigate the geometry (Geometric Characterization of SCFD Whiskers section) and processing–structure–property relationship (Structure–Property Relationship of SCFD Whiskers section) of these whiskers, and demonstrate that the SCFD whiskers exhibit improved sensing performance compared with a cylindrical filament (Performance of SCFD Whiskers as Sensors section).

Development of manufacturing methods and materials

Several combinations of manufacturing methods and materials to create tapered whiskers were investigated. Injection molding,[45] vacuum-assisted micromolding,[46] and FDM were three of the established manufacturing procedures identified as potentially suitable to produce tapered whiskers. An additional new method was developed, SCFD. The four materials selected from Table 1 were analyzed to determine their mechanical properties and processability.

The success of the possible manufacturing methods depends on the resulting material and geometric properties of the whisker and the capital cost of the manufacturing procedure. The overarching goal is a scalable manufacturing process/material combination to create a tapered fiber mimicking the mechanical properties of a real rat whisker at minimal cost, while also maintaining the appropriate properties. Finally, we also evaluated whether a process could improve whisker quality and could be scaled to produce multiple whiskers in parallel.

All three traditional manufacturing options tested were found to have significant drawbacks as discussed further in Alternative Manufacturing Options section of the Supplementary Data S1. Therefore, a specialized manufacturing method, we call SCFD, was developed to manufacture the artificial whiskers and is described in detail. SCFD successfully produced artificial whiskers (Fig. 3a) with the geometry specified in Figure 1c.

SCFD is inspired by conventional drawing techniques that are used to produce fibers with constant diameters.[47,48] However, in the production of uniform fibers the ''transition'' region created as the fiber narrows is minimized and removed from the final product. In this study, SCFD is specifically developed to exploit the transition region that occurs during a drawing process to maximize and control the whisker's taper profile. SCFD consists of the following steps that are illustrated in Figure 3b:

1. Top schematic: The filament is clamped at one end, while the other end is pulled across a heated Teflon surface ($t=0$).
2. Middle schematic: If the filament is heated sufficiently past the T_g of the polymer, the filament that is in contact with the surface is drawn by a pulling force. A small mass (10–50 g) attached to the end of the filament applies a constant force, which in turn controls the drawing rate.
3. When the filament loses contact with the surface, it cools below its T_g and maintains the newly drawn shape and forms the tapered whisker.
4. Bottom schematic: The filament that remains on the surface is drawn further, causing a taper to be formed as the whisker is pulled across the surface.

Several manufacturing parameters were identified to affect whisker geometry, as schematized in Figure 3b. These parameters include the temperature of the surface (T_s), the rate and acceleration of the pulling motion (v_P, a_P) as a result of the applied force, the drawn length of the whisker (ΔL), and the heated length (L_H). As the whisker draws, the cross-sectional area reduces. As such, a smaller force is required to maintain the drawing process. When the applied force exceeds the tensile strength of the filament at T_s, the filament breaks. As such, the applied force influences the tip diameter.

The next step was to ensure the different selected polymers could sustain the desired range of motion. Finite element analysis (FEA) (Finite Element Analysis of Whisker Deflection section in Supplementary Data S1) was used to model the strains induced within the whisker to sustain a deflection at the upper limit of what is observed in a biological rat during whisking.[19]

To examine the quasistatic elastic behavior of the four polymers, thick film samples of the specimens were loaded at a constant strain rate of $0.05\,s^{-1}$ in a DMA. The resulting stress–strain plots are shown in Figure 3c. The ultimate tensile strain of all four materials far exceeds the 0.66% max strain predicted in Supplementary Figure S2 by FEA for a 60° deflection, suggesting that all materials have a sufficient range of elastic behavior to cope with deflections that are sustained by biological vibrissae as measured by Williams and Kramer.[19] However, the ABS demonstrates mild nonlinear elastic behavior, which is expected to convolute the relationship between deflection and any reaction forces or moments at the base of a whisker made from the ABS.

The Young's modulus (Fig. 3c, inset) is calculated by measuring the slope from 0% to 1% strain. The elastic properties measured from Figure 3 are summarized in Table 3. The high elongation at break for PC-Max indicates that it exhibits large amounts of plastic deformation compared with the standard PC, likely due to plasticizers added to improve the processability of PC.

Although all four polymers exhibited properties that suggest they could sustain deflections similar to a biological rat vibrissa (Supplementary Fig. S2b), the conventional PC and polysulfone were found to be unsuitable for SCFD, the only manufacturing method identified to reliably produce the desired geometry at low cost. The polysulfone required excessive heating before drawing due to its high T_g. The PC became brittle and fractured prematurely, leaving PC-Max and the ABS as the remaining materials suitable for production of whiskers.

To determine which of the remaining polymers were best suited for SCFD, the viscoelastic properties of ABS and PC-Max were investigated to establish the glass transition temperature for the materials and quantify the mechanical performance at room and elevated temperatures. Figure 3d plots the storage modulus (E'), loss modulus (E''), and tan δ for

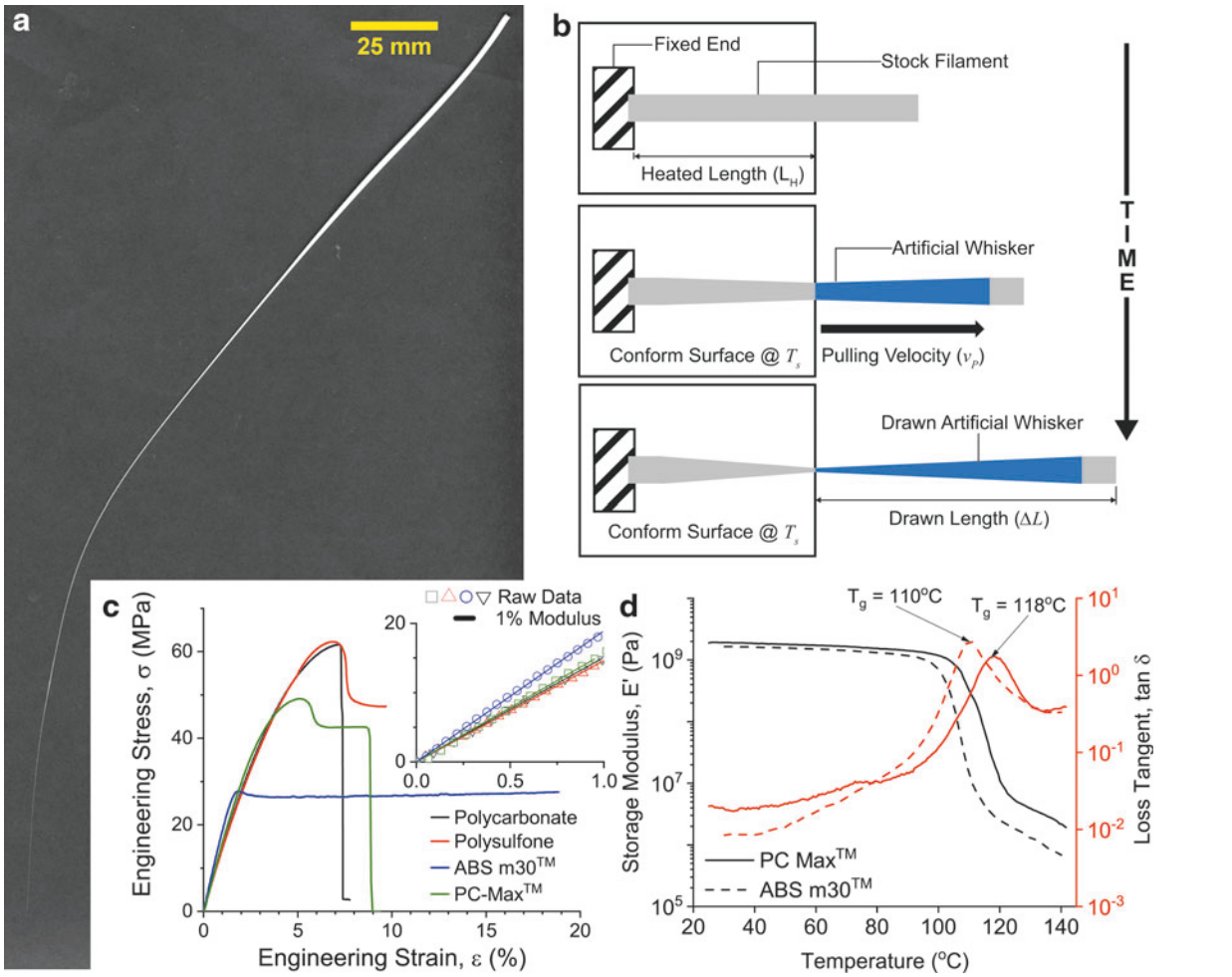

FIG. 3. Schematic of SCFD manufacturing method and the mechanical properties of possible materials. **(a)** SCFD-produced whisker with geometric properties in the desired range. **(b)** Time course of whisker drawing. From *top* to *bottom* the schematics show the initial position of a filament before drawing; the whisker after drawing for some time; and the whisker after continued drawing. Once the desired tip diameter is achieved, the whisker can be trimmed. **(c)** Stress–strain curves of thick film specimen under tensile load at room temperature (25°C). *Inset*: 1% modulus linear fit for each of the materials tested. **(d)** Viscoelastic properties of the ABS and PC-Max film specimens at temperatures that range between 25°C and 140°C under a 1 Hz oscillating load. SCFD, surface conforming fiber drawing. Color images are available online.

ABS and PC-Max at temperatures that range between room temperature and 140°C. The experiments were performed as temperature sweeps at a constant frequency of 1 Hz. The T_g, as defined by peak of tan δ, is similar for both the ABS ($\approx$110°C) and the PC-Max ($\approx$118°C). The T_g for both materials is much higher than room temperature, and both materials have a comparatively low loss modulus compared with the storage modulus at temperatures <80°C. The combination of low loss modulus and high glass transition temperature suggests that both materials will have a fast response time after deflection and will return to the original position quickly in a range of operating conditions. The loss tangent of the PC-Max at room temperature (tan $\delta \approx 0.02$) is within the range of measured loss tangent values for keratin[37] (tan $\delta = 0.02 \leftrightarrow 0.03$), whereas the loss tangent of ABS is lower (0.008). Therefore, with all else being equal, a whisker manufactured from PC-Max will exhibit a closer dynamic response to the biological vibrissae. In addition, the loss tangent profile of the PC-Max varies less with temperature than the ABS, suggesting that a PC-Max whisker will exhibit

TABLE 3. MEASURED ELASTIC PROPERTIES OF THE FOUR SELECTED POLYMERS

Material	*1% Elastic modulus (GPa)*	*1% Modulus residual (Pa)*	*Ultimate tensile strain (%)*	*Ultimate tensile strength (MPa)*	*Elongation at break (%)*
Stratasys ABSplus	1.89	1.5*e*12	2.2	49.1	8.7
Polymaker PC-Max	1.56	7.7*e*11	5.2	28.5	43.8
Polycarbonate	1.51	6.1*e*11	7.2	61.6	7.3
Polysulfone	1.46	7.4*e*11	6.9	62.3	9.7

more predictable and consistent dynamic properties than an ABS whisker for a larger range of time and temperature scales. As a result of the analysis, the PC-Max PC was chosen as the material to be used with SCFD in this study.

As evidenced by the given examples, the challenge in manufacturing biomimetic artificial whiskers has been the trade-off between the required geometry and material properties, the strength of the final product and the limitations of processing methods. The choice of thermoplastic polymers as the material class of interest is the result of the required density, elastic modulus, and intrinsic damping to match the biological vibrissae. Some polymers, such as low-density polyethylene, are formable and draw easily but are not sufficiently elastic and stiff to function as a whisker material. Stiffer more brittle thermoplastics can plastically deform or fatigue during operation. As soft robotics becomes more prevalent, understanding the dynamic and static behavior of polymers in response to inputs and loads becomes a crucial part of characterizing the overall performance of a robotic system.

Geometric characterization of SCFD whiskers

To test the ability of the SCFD to replicate the geometry of biological whiskers, the rostral (short) and caudal (long) whiskers of a Long Evans rat were targeted for replication at $5\times$ scale. The dimensions required to successfully replicate rostral and caudal whiskers with a suitable $Slope_R$ (Eq. 1) at the $5\times$ scale are provided in Table 4. Rostral and caudal whiskers differ in both size and shape (intrinsic curvature); however, in this study we neglect intrinsic curvature (all whiskers are straight). Thus, the arclength S and the straight-line length L are equal and are simply denoted as S.

To produce the whiskers, the applied load and heated length were optimized for each type of whisker and then filaments were drawn by suspending a weight from the free end of the filament. The location of the desired base diameter was identified along with the desired whisker length, and the drawn filament was then trimmed. An example of one of the rostral whiskers produced is given in Figure 4a. To quantify the whisker profile, the image was binarized (Fig. 4b) with the Phansalkar local thresholding method[49] in ImageJ and then skeletonized to trace the whisker profile.

Using the skeletonized profile as a path, a Euclidean distance transform was conducted to extract the whisker diameter as a function of whisker length (Fig. 4c, d). The $Slope_R$ is calculated for a range of the produced artificial whiskers and is found to fall within the required range to be a successful mimic of the biological rat whisker (Fig. 4e, f) geometry. As the base diameter and whisker length was held constant within both whisker archetypes, variance in the $Slope_R$ is the result of changes in the tip diameter and taper profile.

The profiles of the produced whiskers were not typically perfectly linear (Fig. 4c, d), likely due to manufacturing parameters varying over the drawing step, or due to the nonlinear drawing behavior of the material. In the case of the artificial caudal whiskers, the taper is initially very nonlinear within 25 mm of the base. Adjustments and improved force control of the manufacturing process is expected to improve the linearity of the whisker profile.

In addition, the upper range (>0.0015) of $Slope_R$ values exhibited by biological whiskers cannot yet be reproduced in SCFD whiskers due to the lower limit in tip diameter achievable with the current drawing mechanism. In its current iteration, SCFD cannot apply the very small loads required to prevent tip fracture below $\approx 20\,\mu$m while continuing to draw the whisker. Continued development of the drawing apparatus should extend the range of demonstrable $Slope_R$ at the $5\times$ scale. Images of the artificial whiskers analyzed in Figure 4e and f are compiled in Supplementary Data S2.

As required by the specifications listed in Figure 2, artificial whiskers produced at the $5\times$ scale through SCFD must deflect through 50° and return to their original profile. To test the deflection behavior, a smooth metal disk (Fig. 4g) was used to test the deflection behavior along the length of the whisker while the whisker base was fixed. Initial testing showed that whiskers with the required dimensions made from PC-Max were able to undergo a >50° deflection before rapidly returning to their predeformed state as predicted by the FEA and material testing. Plastic deformation was observed after an $\sim 82°$ deflection.

Structure–property relationship of SCFD whiskers

The mechanical properties of an artificial whisker are central to its performance and function. The predominant static load experienced by the whisker is expected to be in bending as whiskers will deflect during contact with surfaces. To investigate if a whisker produced through SCFD varies in mechanical properties along its length as a result of drawing, 15 mm long samples were obtained from three locations along the length of a PC-Max whisker (Fig. 5a) and oscillated under three-point bending conditions. The samples were chosen so that the loading point for each test was at 50, 100, and 150 mm from the base of the whisker.

It is noted that the cross section is not constant throughout each sample due to the taper, but the measured moduli relative to a baseline provide a means for assessing relative trends. To provide the baseline, we measured the storage modulus at room temperature of a stock cylindrical filament of PC-Max under three-point bending, which was found to be ≈ 1.9 GPa at a strain amplitude of 1% across multiple samples.

Figure 5b shows modulus results obtained at the three specified locations across three whiskers. The measured

Table 4. Desired Artificial Whisker Dimensions

Dimension	*Rostral biological*	*Caudal biological*	*Rostral artificial (5×)*	*Caudal artificial (5×)*
Whisker length (S)	20 mm	50 mm	100 mm	250 mm
Base diameter (D_{base})	75 μm	175 μm	375 μm	875 μm
Tip diameter (D_{tip})	$\approx 3 \leftrightarrow 5\,\mu$m	$\approx 3 \leftrightarrow 5\,\mu$m	$\approx 25\,\mu$m	$\approx 25\,\mu$m

Targeted geometry to produce caudal and rostral whiskers that are geometrically similar to biological specimens at the $5\times$ scale.

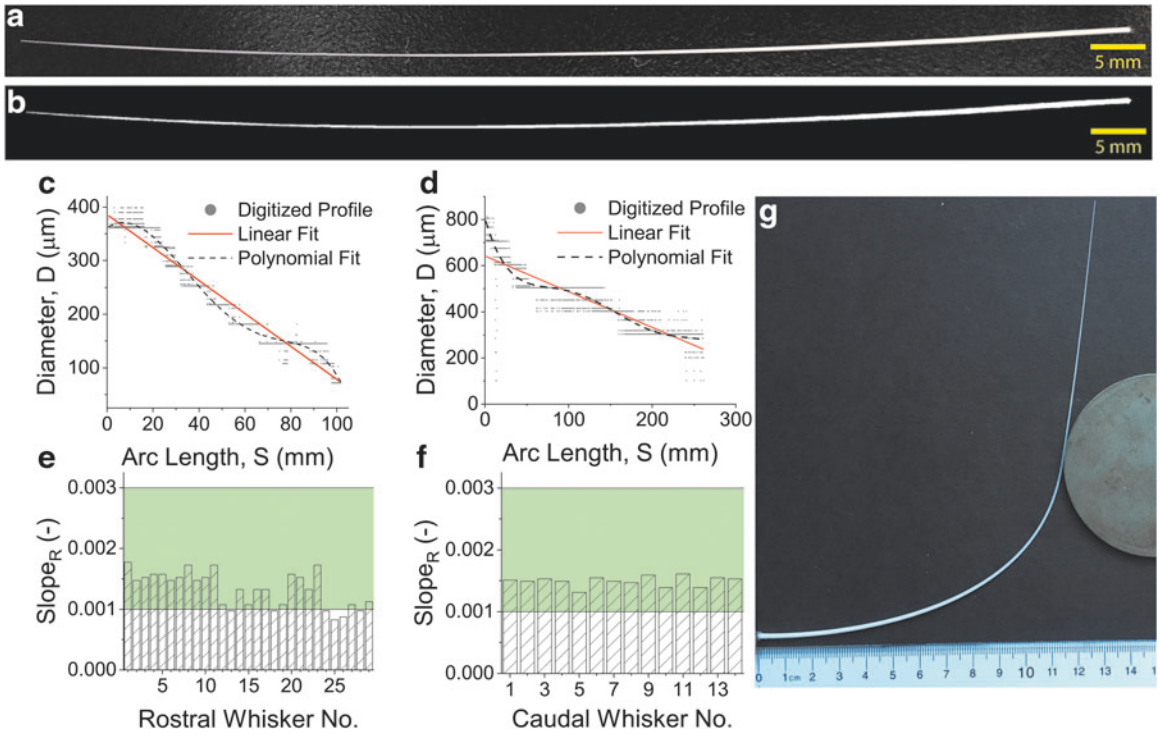

FIG. 4. Geometric characterization of manufactured whiskers. **(a)** Image of a manufactured rostral whisker at the 5× scale. **(b)** A binarized version of a rostral whisker ready of analysis. **(c)** A digitized profile of a rostral whisker. **(d)** A digitized profile of a caudal whisker. The digital profile is the result of the measured whisker diameter discretized into discrete values based on pixel resolution. **(e)** The resulting $Slope_R$ values for a range of manufactured rostral *whiskers*. **(f)** The resulting $Slope_R$ for a range of manufactured caudal whiskers. **(g)** SCFD whisker during an ∼82° deflection at which point plastic deformation begins to occur. The whisker is able to undergo large deflections elastically with the base rigidly fixed. Each mark on the ruler is 1 mm. The whisker geometry depicted is at 10× scale to be compatible with the artificial sensor described in Materials and Methods section. Color images are available online.

storage modulus is larger for samples taken further away from the base of the whisker across multiple, replicate samples, with a 37% increase measured between samples taken near base versus tip (50 vs. 150 mm).

The increase of storage modulus may be explained in part by alignment of polymer chains during drawing.[50] Nanoscale analysis was conducted to confirm whether this may be the only contributing factor, or whether additional mechanisms were contributing to the significant stiffening. AFM analysis (Fig. 5c) suggests that the PC used initially consists of multiple phases with a matrix and soft particles ∼200 nm in diameter dispersed throughout. At the locations examined, the microstructure near the base of drawn whiskers was similar to the microstructure in the stock filament (Fig. 5d), as such images of microstructure at the whisker base are not included here. Near the tip of a drawn whisker, the cross section is devoid of the soft filler phase (Fig. 5d), providing a potential explanation for the increase in observed bending modulus near the whisker tip.

Although the drawing process stiffens the whisker (Fig. 5b) such that the whisker modulus is within the desired range (2 ↔ 4 GPa) required by the design brief (Fig. 2c), the manufactured whisker has a gradient in mechanical properties and is expected to behave differently under deflection compared with a whisker with homogeneous material properties. The difference in deflection behavior must be accounted for by the sensor electronics associated with the whisker since the whisker geometry and compliance is used to provide a unique mapping of contact location. The gradient in mechanical properties is accounted for by training a machine learning algorithm on a set of data from the manufactured whiskers (Performance of SCFD Whiskers as Sensors section). A change in modulus convolutes the response of a whisker to deflection and, if the change in modulus is dependent on the exact parameters used from the drawing step then multiple whiskers in an array may have varying material properties depending on their exact length and taper.

Although biological vibrissae also have an apparent change in bending modulus along their length, for robotic applications the preference would be to control the modulus along the entire length of the artificial whisker so that all whiskers maintain the same mechanical properties along the whisker length no matter the geometry. The change in microstructure (Fig. 5c, d) is hypothesized to be the result of two mechanisms: particle coalescence[51,52] and migration.[53,54] Future study will further examine the processing–structure–property relationship of SCFD whiskers as well as annealing steps postdrawing that may help homogenize the material properties of the drawn whisker.

Performance of SCFD whiskers as sensors

A recent simulation study has shown that for a tapered whisker there is a unique, one-to-one relationship between the 3D contact point (r_{cp}, θ_{cp}, Φ_{cp}) and the triplet of mechanical signals (M_B, M_D, F_X) at the whisker base.[12] The mapping is unique and one-to-one regardless of whether the

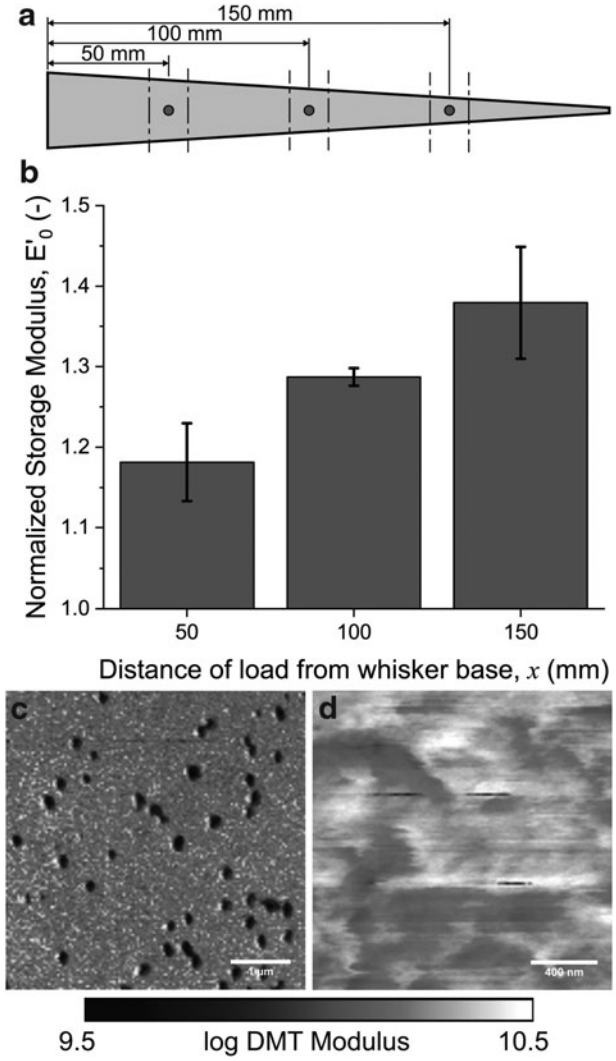

FIG. 5. Local bending modulus along whisker length. **(a)** Discretization of an artificial whisker for analysis of local variance in bending stiffness. *Dashed black lines* indicate the locations at which the whisker was cut to form the three-point bending samples at least 14 mm in length. *Blue circles* indicate the load point during experiments. Whisker is not drawn to scale. **(b)** Normalized storage modulus profile (taken at 25°C) along the length of several whiskers manufactured from PC-Max through SCFD. The storage modulus profiles are normalized to the storage modulus measured for a cylindrical sample of PC-Max ($E_0 = 1.9$ GPa). The storage modulus was averaged for multiple strain amplitudes between 0.2% and 1.0% across three samples. **(c)** PeakForce™ QNM image of the filler phase within stock filament. The strong contrast between the filler phase and the matrix indicates the filler is much softer than the polycarbonate matrix. **(d)** At a cross section close enough to the tip, no distinct filler phase remains in a Peakforce™ QNM image, with only relatively minor variations in matrix modulus observed.

whisker has intrinsic curvature, provided that the whisker is sufficiently tapered. The mapping is nonunique for a cylindrical whisker.[12]

The production of the SCFD tapered whiskers allows us to confirm these simulation results in hardware. Specifically, we performed 3D contact point determination using both a PC-Max tapered whisker manufactured through SCFD and a cylindrical whisker also made from PC-Max. The behavior of an SCFD whisker under repeated and long-term loading was also examined in Cyclic Testing of Voltage Output Stability Under Continuous Loading section of the Supplementary Data S1.

We began by replicating the hardware experiment in simulations. We ran deflection simulations of whiskers that had the same dimensions as the tapered and cylindrical hardware whiskers. The set of contact points used in simulation not only included those used in experiments but also included contact points located between those used experimentally. In other words, the simulations were run at a higher spatial resolution than the experiments. The results of these simulations are in Figure 6a and 6b. The three radii (r_{cp}) tested are represented in three separate colors and labeled as r_1–r_3.

In Figure 6a, the simulated axial force is plotted as a function of the bending magnitude for tapered and cylindrical whiskers. In the panels of this subplot, it is immediately evident that the tapered whisker generates surfaces with clear separation between them, whereas the cylindrical whisker generates surfaces that overlap. The insets for both panels in Figure 6a show expanded views of the smallest values of bending magnitude and axial force, at an aspect ratio of 8:1. The surfaces of the tapered whisker still exhibit clear separation, even for these small magnitude signals. In contrast, the surfaces for the cylindrical whisker are not separated, indicating that—as predicted by previous numerical results—the cylindrical whisker does not permit a unique mapping between contact point location and the mechanical signals.

Similar results were found when bending direction was plotted as a function of bending magnitude, as shown in Figure 6b. In both panels, the four separate surfaces represent the four quadrants for bending direction. The insets again show that the tapered whisker generates distinct separated surfaces, whereas the cylindrical whisker generates surfaces that overlap, evident as mixed coloring. Again, these simulation results indicate that the cylindrical whisker will not be able to uniquely predict all contact point locations.

In Figure 6c, we further quantified the separation of the surfaces for both the tapered and cylindrical whisker. We calculated the difference in axial force between two of the three surfaces shown for each whisker in Figure 6a (r_1–r_2 and r_2–r_3). For the tapered whisker, the separation of the surfaces continuously increases. In contrast, the separation between the surfaces for the cylindrical whisker is negligible, oscillating around zero. This result further indicates that a unique mapping between the mechanical signals and 3D contact point for the tapered whisker is obtainable, but not for the cylindrical whisker. We next used the mappings generated in simulation as a lookup table for mechanical data acquired experimentally.

We recorded (M_B, M_D, F_X) at the base of each whisker as it was deflected to 192 unique 3D positions (see Materials and Methods section). After excluding small angles (θ_{cp} or Φ_{cp} <5°), the data set contained 120 unique 3D positions. We chose to exclude 3D positions with angles <5° after experimentally determining that these small deflections led to high prediction errors as discussed in Emnett *et al.*[11] At a given position along its length, the tapered whisker has a smaller second moment of area compared with the cylindrical

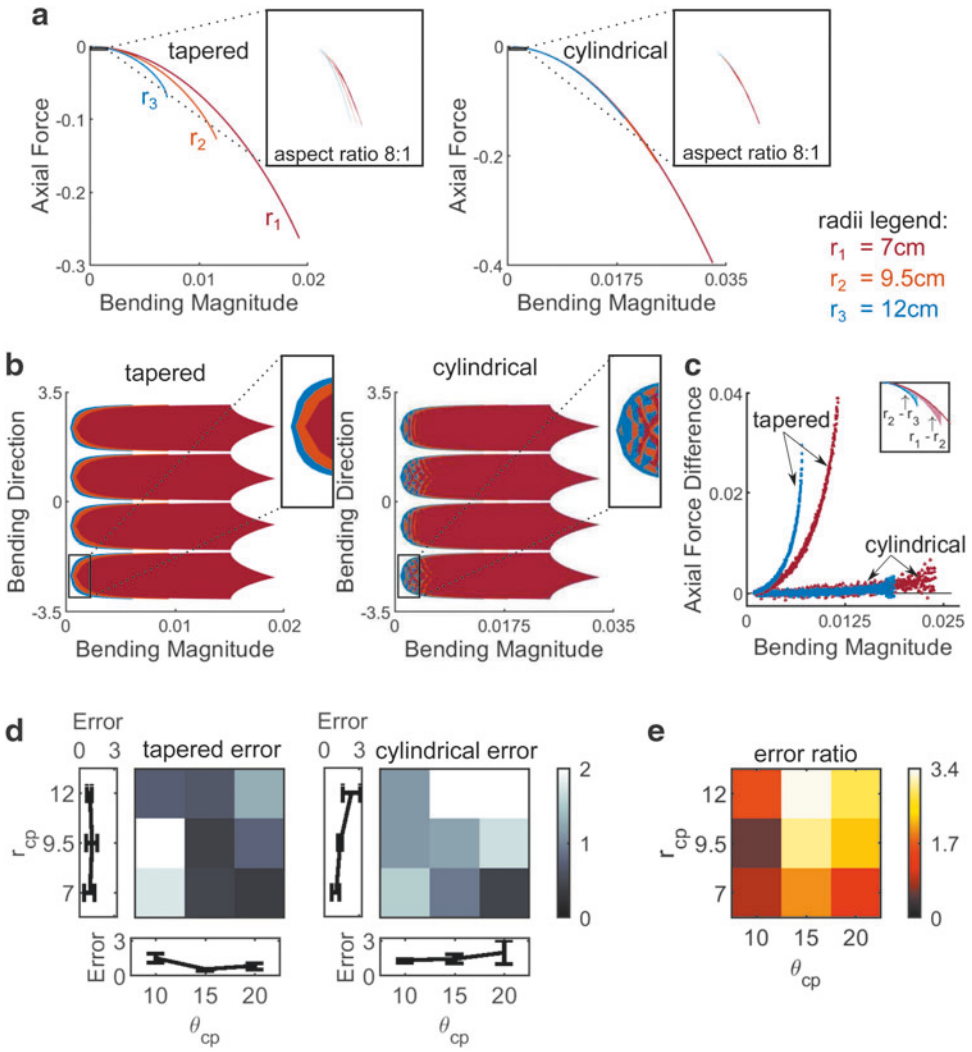

FIG. 6. Performance analysis for cylindrical and tapered *whiskers*. **(a, b)** 3D simulation results for deformations of tapered and cylindrical whiskers. Each subplot shows a 2D projection of the 3D surface formed by (M_B, M_D, F_X). The colors correspond to the three different radii tested. *Red*: $r_1 = 7.0$ cm; *Orange*: $r_2 = 9.5$ cm; *blue* $r_3 = 12$ cm. **(a)** Axial force versus bending magnitude for deformations of tapered and cylindrical whiskers. These plots are difficult to visualize at this angle, so lines were superimposed over the surface ''edges.'' Both *insets* have an 8:1 aspect ratio and show expanded views in the *boxed* region. In these *insets*, lines were not superimposed over the surface edges. For the tapered whisker, surfaces are distinct, indicating a unique mapping between radial position and mechanical signals. In contrast for the cylindrical whisker, surfaces are stacked on top of each other, indicating a nonunique mapping. **(b)** Bending direction versus bending magnitude for deformations of tapered and cylindrical whiskers. Both panels contain four distinct surfaces, reflecting the four quadrants for bending direction. *Insets* show expanded views of the *boxed* regions and have the same aspect ratio as the main figures. For the tapered whisker, colors are separated into distinct bands, indicating separate surfaces and thus a unique mapping. In contrast, colors are mixed for the cylindrical whisker, indicating a nonunique mapping. **(c)** Quantification of separation between tapered surfaces and separation between cylindrical surfaces in **(a)**. For bending magnitude in **(a)**, the difference in axial force between two of the three surfaces is plotted (r_1–r_2 and r_2–r_3). As bending magnitude increases, the surface separation for the tapered whisker increases, but the separation for the cylindrical whisker oscillates near zero. **(d, e)** Euclidean distance errors (cm) between predicted and actual 3D contact point locations are quantified across the full data set (i.e., θ_{cp} and $\Phi_{cp} > 5°$). **(d)** Mean distance errors for tapered and cylindrical whiskers are plotted for r_{cp} and θ_{cp}. Color in each square indicates the mean distance error averaged for all values of Φ_{cp}, for the designated values of r_{cp} and θ_{cp}. For the tapered whisker, the largest mean error occurs at small radial distances and angles. For the cylindrical whisker, the largest mean error occurs at large radial distances and angles. Marginals show mean ± standard error of the mean error as functions of r_{cp} (*left panels*) and of θ_{cp} (*bottom panels*). **(e)** The ratio of cylindrical whisker error to tapered whisker error (indicated by the color bar). Large values indicate that the tapered whisker was more accurate than the cylindrical whisker. Color images are available online.

whisker. The tapered whisker is thus more easily deformed for a given deflection, reducing the reaction moment at the base. Therefore, at small deflection angles the strain induced in the cross sensor is not large enough to overcome the sensor noise, reducing accuracy for the tapered whisker. We used the mechanical signals (M_B, M_D, F_X) as input to the mapping, generated through Random Forest Regression on the simulation results, and predicted the 3D contact point. Error for each point was computed as the (unsigned) distance between the actual 3D contact point and the predicted 3D contact point.

As seen in Figure 6d, the tapered whisker demonstrates a smaller error than does the cylindrical whisker across most 3D contact points. The ratio of the error generated by the cylindrical whisker to the error generated by the tapered whisker is shown in Figure 6e. This error ratio is greater than one in all regions of the plot except for the bottom two squares in the first column, and is highest in the top right region of the plot. These results indicate that the tapered whisker offers a particularly large performance advantage compared with the cylindrical whisker for large values of r_{cp} and θ_{cp}. The median of the distance error for the tapered whisker and cylindrical whisker, respectively, is 0.57 (interquartile range [IQR] = 0.81) and 1.3 (IQR = 1.48).

Further inspection of the data in Figure 6d and 6e shows that many of the large error values for the tapered whisker lie at the smallest values of θ_{cp}, whereas, in contrast, large error values for the cylindrical whisker are more broadly distributed across a range of angles. We therefore predicted that the performance advantage of the tapered whisker could be further enhanced by excluding angles <10° (θ_{cp} and $\Phi_{cp} < 10°$). This additional exclusion is tantamount to increasing the range of the sensor ''dead band,'' which we had previously anticipated (see Materials and Methods section) would be $\sim 5°$. Consistent with expectations, omitting these angles improved the median distance error for the tapered whisker to 0.53 (IQR = 0.61, $n = 104$), but did not change the median distance error for the cylindrical whisker.

Discussion and Conclusion

A novel manufacturing process termed surface conforming fiber drawing (SCFD) has been developed for the manufacture of artificial whiskers that is a biomimetic of the tapered geometry and mechanical properties of a biological rat vibrissae. SCFD is a viable technique to produce tapered filaments from suitable thermoplastics for a variety of applications. SCFD whiskers are strong, flexible, and have mechanical properties that are close to those of the biological rat vibrissae. Compared with previous solutions, SCFD whiskers demonstrate higher aspect ratios and finer tip diameters ($\approx 30\,\mu$m) than what has been previously presented in the literature. In addition, SCFD-produced whiskers can undergo large deflections repeatedly due to being manufactured from a single piece of PC filament. SCFD also creates a smooth consistent taper near the whisker tip.

The drawing of the whisker is shown to induce a gradual change in the microstructure of the whisker, which results in a $\approx 40\%$ increase in bending modulus along the length of the whisker. The observed increase in bending modulus did not prevent the whisker from successfully providing contact point prediction. SCFD whiskers when compared against cylindrical counterparts were shown to have improved contact point predictive abilities. The median distance error predicted for SCFD whiskers was only 0.57 cm as compared with 1.3 cm for a cylindrical whisker of the same material. This finding suggests that SCFD tapered whiskers offer the ideal solution for artificial tactile whisker arrays over cylindrical options.

At present, the ability of SCFD to repeatedly produce a specific desired geometry within tight tolerances is limited, but automation and a detailed parametric analysis of the manufacturing process will provide a path for future development along these lines.

Author Disclosure Statement

D.W. Collinson, M.J.Z. Hartmann and L.C. Brinson currently have a patent (Application No. US16/102,364) titled ''Processing methods and apparatus to manufacture a functional, multi-scale, tapered fiber from polymer filament'' pending to Northwestern University. The patent application makes a claim to the manufacturing procedure used to form the artificial vibrissae.

Funding Information

This multiyear research effort was sequentially supported by grants from the National Science Foundation (NSF): award numbers EFRI-0938007 (Liu, PI), IIS-1208118, and IOS-1558068 to M.J.Z.H.; and finally BCS-1734981 to M.J.Z.H. and L.C.B. D.W.C. was partially supported by the Goodyear Tire and Rubber Company, Fulbright Science and Innovation Fellowship, the John R Templin Fellowship and the Ryan Fellowship from the International Institute for Nanotechnology. H.M.E. was partially sponsored by individual NSF GFRP award DGE-1324585. This study made use of the SPID and EPIC facilities of Northwestern University's NUANCE Center, which has received support from the Soft and Hybrid Nanotechnology Experimental (SHyNE) Resource (NSF ECCS-1542205); the MRSEC program (NSF DMR-1720139) at the Materials Research Center; the International Institute for Nanotechnology (IIN); the Keck Foundation; and the State of Illinois, through the IIN.

Supplementary Material

Supplementary Data S1
Supplementary Data S2
Supplementary Figure S1
Supplementary Figure S2
Supplementary Figure S3

References

1. Arkley K, Grant RA, Mitchinson B, *et al.* Strategy change in vibrissal active sensing during rat locomotion. Curr Biol 2014;24:1507–1512.
2. Arkley K, Tiktak GP, Breakell V, *et al.* Whisker touch guides canopy exploration in a nocturnal, arboreal rodent, the Hazel dormouse (*Muscardinus avellanarius*). J Comp Physiol A 2017;203:133–142.
3. Brecht M, Preilowski B, Merzenich MM. Functional architecture of the mystacial vibrissae. Behav Brain Res 1997;84:81–97.

4. Carvell GE, Simons DJ. Biometric analyses of vibrissal tactile discrimination in the rat. J Neurosci 1990;10:2638–2648.
5. Guić-Robles E, Valdivieso C, Guajardo G. Rats can learn a roughness discrimination using only their vibrissal system. Behav Brain Res 1989;31:285–289.
6. Hobbs JA, Towal RB, Hartmann MJ. Probability distributions of whisker–surface contact: quantifying elements of the rat vibrissotactile natural scene. J Exp Biol 2015;218:2551–2562.
7. Hobbs JA, Towal RB, Hartmann MJ. Spatiotemporal patterns of contact across the rat vibrissal array during exploratory behavior. Front Behav Neurosci 2016;9:356.
8. Vincent S. The tactile hair of the white rat. J Comp Neurol 1913;23:1–34.
9. Welker W. Analysis of sniffing of the Albino rat 1. Behaviour 1964;22:223–244.
10. Cramphorn L, Ward-Cherrier B, Lepora NF. (Eds). Tactile manipulation with biomimetic active touch. 2016 IEEE International Conference on Robotics and Automation (ICRA), Stockholm, Sweden, May 16–21, 2016. IEEE.
11. Emnett MH, Graff MM, Hartmann MJZ. A Novel Whisker Sensor Used for 3D Contact Point Determination and Contour Extraction. Pittsburgh, PA: Robotics: Science and Systems, 2018.
12. Huet LA, Rudnicki JW, Hartmann MJ. Tactile sensing with whiskers of various shapes: determining the three-dimensional location of object contact based on mechanical signals at the whisker base. Soft Robot 2017;4:88–102.
13. Scholz GR, Rahn CD. Profile sensing with an actuated whisker. IEEE Trans Robot Autom. 2004;20:124–127.
14. Towal RB, Quist BW, Gopal V, *et al.* The morphology of the rat vibrissal array: a model for quantifying spatiotemporal patterns of whisker-object contact. PLoS Comput Biol 2011;7:e1001120.
15. Kim D, Möller R. Biomimetic whiskers for shape recognition. Robot Auton Syst 2007;55:229–243.
16. Deer W, Pounds PEI. Lightweight whiskers for contact, pre-contact, and fluid velocity sensing. IEEE Robot Autom Lett 2019;4:1978–1984.
17. Schultz AE, Solomon JH, Peshkin MA, et al. (Eds). Multifunctional whisker arrays for distance detection, terrain mapping, and object feature extraction. In: 2005 ICRA 2005 Proceedings of the 2005 IEEE International Conference on Robotics and Automation, Barcelona, Spain, April 18–22, 2005. IEEE.
18. Solomon JH, Hartmann MJ. Biomechanics: robotic whiskers used to sense features. Nature 2006;443:525.
19. Williams CM, Kramer EM. The advantages of a tapered whisker. PLoS One 2010;5:e8806.
20. Evans M, Fox CW, Pearson MJ, et al. Spectral template based classification of robotic whisker sensor signals in a floor texture discrimination task. In: Kyriacou T, Melhuish C, Witkowski M, eds. Proceedings TAROS, Londonderry, United Kingdom. Ulster, UK: Ulster University Press; 2009;19–24.
21. Fox CW, Mitchinson B, Pearson MJ, *et al.* Contact type dependency of texture classification in a whiskered mobile robot. Auton Robots 2009;26:223–239.
22. Pearson MJ, Pipe AG, Melhuish C, *et al.* Whiskerbot: a robotic active touch system modeled on the rat whisker sensory system. Adapt Behav 2007;15:223–240.
23. Sullivan JC, Mitchinson B, Pearson MJ, *et al.* Tactile discrimination using active whisker sensors. IEEE Sens J 2012;12:350–362.
24. Ou J, Dublon G, Cheng C-Y, *et al.* Cilllia-3D Printed Micro-Pillar Structures for Surface Texture, Actuation and Sensing. CHI; San Jose, CA: Association for Computing Machinery, 2016.
25. Ward J, Austin R, Genovese A, inventors; Ametek Inc., assignee. Hollow Tapered Brush Bristles. U.S.A. patent US4307478A. 1981.
26. Smith AF, inventor; E. I. du Pont de Nemours & Company, assignee. Artificial Filament. U.S.A patent US2341823A. 1944.
27. Liu X, Sun N, Wang M, inventors; du Pont de Nemours and Company, assignee. Tapered filaments from bio-based materials and methods for preparing same patent WO2009097600A1. 2009.
28. Adineh VR, Liu B, Rajan R, *et al.* Multidimensional characterisation of biomechanical structures by combining Atomic Force Microscopy and Focused Ion Beam: a study of the rat whisker. Acta Biomater 2015;21:132–141.
29. Belli H, Yang AE-T, Bresee C, *et al.* Variations in vibrissal geometry across the rat mystacial pad: base diameter, medulla, and taper. J Neurophysiol 2017;117:1807–1820.
30. Kan Q, Rajan R, Fu J, *et al.* Elastic modulus of rat whiskers-A key biomaterial in the rat whisker sensory system. Mater Res Bull 2013;48:5026–5032.
31. Voges D, Carl K, Klauer GJ, *et al.* Structural characterization of the whisker system of the rat. IEEE Sens J 2012;12:332–339.
32. Chernova O, Kulikov V. (Eds). Structural differences between the shafts of mammalian vibrissae and hairs and their causes. Dokl Biol Sci 2011;438:182–185.
33. Hobbs JA, Towal RB, Hartmann MJZ. Evidence for functional groupings of vibrissae across the rodent mystacial pad. PLoS Comput Biol 2016;12:e1004109.
34. Carl K, Hild W, Maempel J, *et al.* Characterization of statical properties of rat's whisker system. IEEE Sens J 2012;12:340–349.
35. Herzog E, Bahr D, Richards C, *et al.* Spatially dependent mechanical properties of rat whiskers for tactile sensing. MRS Online Proc Library Arch 2004;844:Y3.6/R3.6.
36. Quist BW, Faruqi RA, Hartmann MJ. Variation in Young's modulus along the length of a rat vibrissa. J Biomech 2011;44:2775–2781.
37. Druhala M, Feughelman M. Dynamic mechanical loss in keratin at low temperatures. Colloid Polym Sci 1974;252:381–391.
38. Melchels FP, Domingos MA, Klein TJ, *et al.* Additive manufacturing of tissues and organs. Prog Polym Sci 2012;37:1079–1104.
39. Wong KV, Hernandez A. A review of additive manufacturing. ISRN Mech Eng 2012;2012:208760.
40. Labrecque L, Kumar R, Dave V, *et al.* Citrate esters as plasticizers for poly (lactic acid). J Appl Polym Sci 1997;66:1507–1513.
41. Rasal RM, Janorkar AV, Hirt DE. Poly(lactic acid) modifications. Prog Polym Sci 2010;35:338–356.
42. Lee HM, Park OO. Rheology and dynamics of immiscible polymer blends. J Rheol 1994;38:1405–1425.
43. Hires SA, Schuyler A, Sy J, *et al.* Beyond cones: an improved model of whisker bending based on measured mechanics and tapering. J Neurophysiol 2016;116:812–824.

44. Huet LA, Schroeder CL, Hartmann MJ. Tactile signals transmitted by the vibrissa during active whisking behavior. J Neurophysiol 2015;113:3511–3518.
45. Heckele M, Schomburg WK. Review on micro molding of thermoplastic polymers. J Micromech Microeng 2004;14: R1–R14.
46. Jeon NL, Choi IS, Xu B, *et al.* Large-area patterning by vacuum-assisted micromolding. Adv Mater 1999;11:946.
47. Courtney JF, inventor; International Harvester Company, assignee. Filament drawing mechanism. United States of America patent US2885257A. 1959.
48. Mummery LR, inventor; E. I. Du Pont de Nemours and Company, assignee. Filament drawing. United States patent US3077004. 1963.
49. Phansalkar N, More S, Sabale A, *et al.* (Eds). Adaptive local thresholding for detection of nuclei in diversity stained cytology images. 2011 International Conference on Communications and Signal Processing (ICCSP), Calicut, India, February 10–12, 2011. IEEE.
50. La Mantia F, Ceraulo M, Mistretta M, *et al.* Effect of hot drawing on the mechanical properties of biodegradable fibers. J Polym Environ 2016;24:56–63.
51. Fortelný I, Živný A. Extensional flow induced coalescence in polymer blends. Rheologica Acta 2003;42:454–461.
52. Janssen JMH, Meijer HEH. Dynamics of liquid-liquid mixing: a 2-zone model. Polym Eng Sci 1995;35:1766.
53. D'avino G, Maffettone P. Particle dynamics in viscoelastic liquids. J Nonnewt Fluid Mech 2015;215:80–104.
54. Tehrani MA. An experimental study of particle migration in pipe flow of viscoelastic fluids. J Rheol 1996;40:1057–1077.

Address correspondence to:
Mitra J.Z. Hartmann
Department of Mechanical Engineering
Northwestern University
Evanston, IL 60208
USA

E-mail: hartmann@northwestern.edu

Lynda Catherine Brinson
Department of Mechanical Engineering
and Materials Science
Duke University
Durham, NC 27708
USA

E-mail: cate.brinson@duke.edu